Batteries & Supercaps

Research Article
doi.org/10.1002/batt.202100401

Chemistry Europe
European Chemical Societies Publishing

www.batteries-supercaps.org

Anisotropic Thermal Characterisation of Large-Format Lithium-Ion Pouch Cells**

Jie Lin,[a] Howie N. Chu,[a, b] Charles W. Monroe,[a, b] and David A. Howey*[a, b]

Temperature strongly impacts battery performance, safety and durability, but modelling heat transfer requires accurately measured thermal properties. Herein we propose new approaches to characterise the heat capacity and anisotropic thermal-conductivity components for lithium-ion pouch cells. Heat capacity was estimated by applying Newton's law of cooling to an insulated container within which the cell was submerged in warmed dielectric fluid. Thermal conductivity was quantified by heating one side of the cell and measuring the opposing temperature distribution with infra-red thermography, then inverse modelling with the anisotropic heat equation. Experiments were performed on commercial 20 Ah lithium iron phosphate (LFP) pouch cells. At 100% state-of-charge (SOC), the heat capacity of a 489 g, 224 mL pouch cell was 541 JK^{-1}. The through-plane and in-plane thermal conductivities were respectively 0.52 and 26.6 $Wm^{-1}K^{-2}$. Capturing anisotropies in conductivity is important for accurate thermal simulations. State-of-charge dependence was also probed by testing at 50% SOC: the heat capacity dropped by 6% and thermal conductivity did not significantly change.

Introduction

Batteries are key enabling devices for the electrification of transport and increased renewable energy generation on the power grid.[1,2] Lithium-ion batteries have improved significantly in cost and energy density[3] and are now the standard energy-storage choice in many applications.[4] Thermal management is an important issue for lithium-ion battery systems, since high temperatures may lead to severe degradation or even catastrophic thermal runaway.[5–7]

For large-format pouch cells operating at high C-rates (a C-rate expresses current, in units of rated cell capacity per charge/discharge duration in hours), high temperatures and spatial temperature non-uniformities may occur depending on the spatial distribution of electrochemical reactions within the cell[8] and the cooling arrangement. This problem has motivated research to develop more thermally conductive electrodes,[9] effective thermal management techniques[10–12] and improved thermoelectrochemical models.[13–17] All of these approaches require accurate knowledge of the cell's heat generation and thermophysical properties. Commercial lithium-ion batteries have a multi-layered unit-cell structure, either in a cylindrical or flat-wound jelly roll or a pouch-style stack, with each unit cell containing current collectors, cathode, anode and separator. This complex combination of materials makes ascertaining the overall thermal properties of the cell a difficult challenge.

Calorimetry is a popular method to characterise the heat capacities of batteries. Commercially available accelerating rate calorimeters[18–20] and differential scanning calorimeters[21,22] are commonly used to measure the specific heat of cells and cell materials. These methods are well documented in American Society for Testing and Materials (ASTM) Standards, such as ASTM E1981 and E537. Apart from this, 'thermal impedance spectroscopy' has also been proposed for heat-capacity measurement at the cell level.[23] Heat flow calorimeters[24] and gradient heat flux sensors[25] have also been used to correlate heat flux with temperature change.

Laser-flash and hot-plate methods have been applied for thermal-conductivity measurement as standard tests in ASTM E1461 and C177, respectively. With these two methods, the commercial xenon flash technique[26] and transient planar source technique[20] are widely used to characterise the thermal conductivities of prismatic cells or layered cell components. The latter is limited to through-plane thermal conductivity characterisation, while the former can also measure the in-plane thermal conductivity by stacking multiple layers of cell components.[27] In addition, photothermal deflection spectroscopy[21,28] has been used to study the thermal conductivity of different cell components, including electrode coatings, current collectors and separators. Thermoreflectance[29,30] can be applied to measure thermal conductivity of thin-film electrodes and solid electrolytes, as well as their interfacial conductances. Similar to the transient planar source technique, a constant-heat-flux method[24,31,32] was also established and showed good stability.

Although there are numerous methods to characterise specific heat and thermal conductivity, some of these may not

[a] Dr. J. Lin, Dr. H. N. Chu, Prof. C. W. Monroe, Prof. D. A. Howey
Department of Engineering Science, University of Oxford,
Oxford, United Kingdom
E-mail: david.howey@eng.ox.ac.uk
[b] Dr. H. N. Chu, Prof. C. W. Monroe, Prof. D. A. Howey
The Faraday Institution, Harwell Campus,
Didcot, United Kingdom

[**] A previous version of this manuscript has been deposited on a preprint server (DOI: https://arxiv.org/abs/2112.09768v1)

Supporting information for this article is available on the WWW under https://doi.org/10.1002/batt.202100401

Research Article
doi.org/10.1002/batt.202100401
Chemistry Europe
European Chemical Societies Publishing

be feasible for large-format lithium-ion pouch cells. In particular, the large aspect ratio and low thermal conductivity make it difficult to maintain an adiabatic environment or uniform temperature for thermal characterisation, thus hindering the direct application of standard calorimetric or air cooling methods.[33,34] Calculating bulk thermophysical properties from mass or volume averages over a cell's interior components could also lead to substantial disagreement with experimental measurements.[20,24]

Here we propose novel thermal characterisation approaches for measuring the effective heat capacity and anisotropic thermal conductivity of large-format lithium-ion pouch cells, as alternatives to existing techniques. For heat capacity quantification, existing techniques often require specialist equipment; for conductivity measurement, they typically do not yield three principal anisotropic components. We apply our novel techniques to quantify the properties of a commercial 20 Ah $LiFePO_4$ (LFP)/graphite pouch cell (AMP20M1HD-A, A123 Systems). Heat capacity is characterised using a cell immersed in a dielectric fluid whose temperature differs from the cell, and modelling the transient temperature response of the cell/fluid system with Newton's law of cooling. The three-dimensional thermal conductivity is obtained by fitting a finite-element thermal model to the surface-temperature response triggered by a constant-temperature input at the rear cell surface. The dynamic temperature evolution was monitored by infrared thermography. A least-squares optimization algorithm was used to parameterise the thermal-conductivity tensor given the previously measured volumetric heat capacity of the battery. Validated with aluminium reference samples, these characterisation methods have the merits of simplicity, speed and accuracy, which is appealing for both scientific research and engineering practice.

Heat-capacity characterisation with the transient cooling technique

Figure 1(a) shows the experimental setup for heat-capacity measurement. A pristine cell at 100% state-of-charge (SOC) was placed in an insulated box (Tundra 35, Yeti) at room temperature, which was used as a calorimeter. The walls of the insulated box contain two polyethylene layers (*ca.* 1 cm thick) surrounding a central layer of polyurethane foam (up to 5.0 cm thick). Dielectric fluid (Thermal H10, Julabo) heated to a specified elevated temperature in a thermal bath (SC100-A25B, Julabo), was added into the box such that the pouch cell was fully immersed, and the box was sealed to minimize the heat loss to the surroundings. Transient temperature responses of the cell and dielectric fluid were recorded via type T thermocouples (Omega Engineering). The thermocouples were calibrated to $\pm 0.1\,^{\circ}C$ absolute accuracy by an ultra precise resistive temperature detector (RTD) (1/10 DIN accuracy, Omega Engineering) before use. Prior to the measurement, a reference test was conducted to measure the temperature response of pure dielectric fluid without a sample cell in the calorimeter.

Since the experimental apparatus is well insulated and the box wall has low thermal conductivity, the system cools predominantly by free convection. Figure 1(b) shows that after a sufficient relaxation time, thermocouples on the battery surface and in the dielectric fluid achieve equal temperatures. After this time, it is reasonable to assume that the box interior achieves a uniform temperature, even when an immersed cell is present.

Assuming that the box interior has uniform temperature T, a general heat balance around the experimental apparatus shown in Figure 1(a) can be formulated as

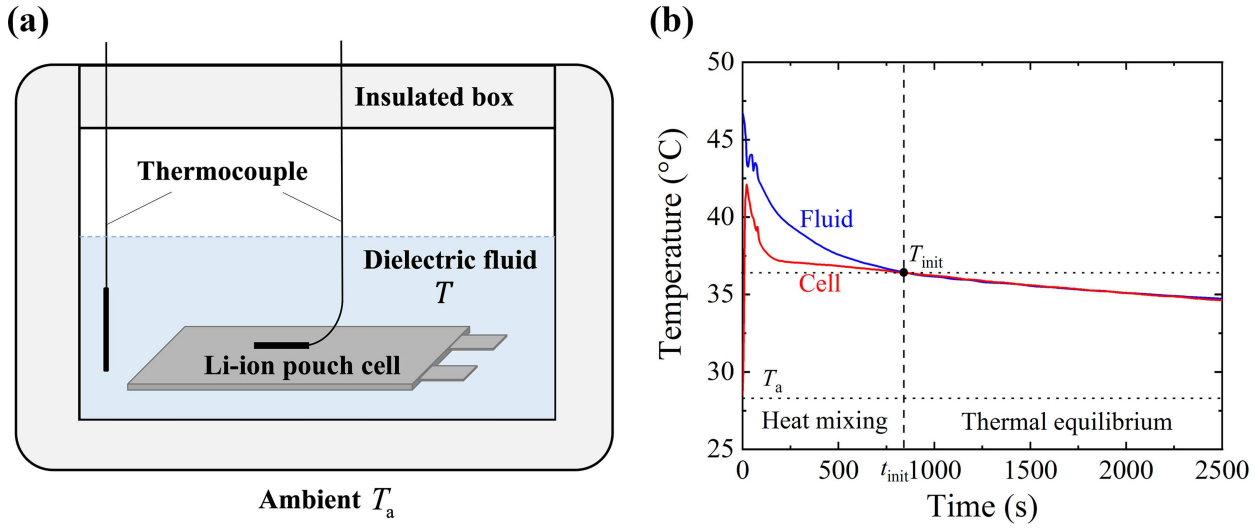

Figure 1. Heat-capacity measurement by transient cooling. (a) Test schematic. (b) Transient temperatures of pouch cell and dielectric fluid, showing the 'Heat mixing' regime at times $t < t_{init}$ and the 'Thermal equilibrium' regime when the temperatures of the battery and dielectric fluid match, at times $t > t_{init}$. The initial temperature T_{init} that appears in equation 3 is also labeled on the figure.

$$C_p^{\text{eff}} \frac{dT}{dt} = -\dot{Q}, \tag{1}$$

in which C_p^{eff} is the lumped total heat capacity of the system (J K^{-1}) and $\dot{Q}$ is the heat flow to the surroundings. The heat flow follows Newton's law of cooling,

$$\dot{Q} = hA[T(t) - T_a], \tag{2}$$

where T_a is the ambient temperature, A is the external surface area of the box available for heat transfer, and h is a heat-transfer coefficient intended to account for both conduction through the box wall and free convection around the box. The solution to this problem is

$$\ln\left(\frac{T(t) - T_a}{T_{\text{init}} - T_a}\right) = -\frac{hAt}{C_p^{\text{eff}}} = -st, \tag{3}$$

so the temperature within the box is expected to decay exponentially with respect to time. Here T_{init} represents the initial temperature after a sufficient equilibration period, represented by the vertical dashed line in Figure 1(b), and parameter s indicates the slope of the temperature decay on a semi-log plot.

The heat-capacity measurement technique exploits the general behaviour modelled by Eq. (3), the fact that h and A are essentially identical between tests, and the fact that similar volumes of dielectric fluid are used in every experiment. Thus if one makes a semilog plot of $T - T_a$ for a reference test without an immersed battery, in which the total heat capacity is C_p^{ref}, and a semilog plot of $T - T_a$ for a test with a battery, in which case the effective total heat capacity of the box is C_p^{test}, the ratio of the slopes of the temperature decay will be

$$\frac{s^{\text{ref}}}{s^{\text{test}}} = \frac{C_p^{\text{test}}}{C_p^{\text{ref}}}. \tag{4}$$

(Note that the intercept of the linear fit, which depends on $\ln(T_{\text{init}} - T_a)$, is not strictly needed when estimating the slopes, so long as h and C_p are relatively constant.) Finally, the battery's heat capacity can be extracted by exploiting the extensivity of total heat capacity, which implies that

$$C_p^{\text{battery}} = \left(\frac{m_f^{\text{ref}} s^{\text{ref}}}{m_f^{\text{test}} s^{\text{test}}} - 1\right) m_f^{\text{test}} \hat{C}_p^{\text{fluid}}, \tag{5}$$

where $\hat{C}_p^{\text{fluid}}$ is the specific heat capacity of the dielectric fluid (taken to be $1.51\ \text{J K}^{-1}\text{g}^{-1}$ here),[35] m_f^j is the mass of the fluid in experiment j, and C_p^{battery} is the total heat capacity of the battery cell. In writing this expression, it has been assumed that both the heat capacity of air in the headspace within the box and that of the box itself are negligible, so that $C_p^{\text{ref}} \approx C_p^{\text{fluid}}$ and $C_p^{\text{test}} \approx C_p^{\text{fluid}} + C_p^{\text{battery}}$. Note that this method also requires that the thermal relaxation of the box wall is fast compared to the rate of bulk cooling.

It should be emphasized that this approach yields the total heat capacity of the battery. Practically it may be more useful to use normalized quantities such as specific heat capacity or volumetric heat capacity. To convert C_p^{battery} to normalized quantities, the mass of a sample cell was measured to be 489.0 g with an analytical balance (IFS 30K0.2DL, Kern & Sohn GmbH), and the cell's exterior dimensions were measured with calipers as $205 \times 155 \times 7.2$ mm. The cell volume was also measured to be $V^{\text{battery}} = 224.0\ \text{cm}^3$ by fluid displacement, which agrees with the caliper measurements within 2%. (Combining the measured mass with the volume measured by liquid displacement yields a bulk cell density of $2.18\ \text{g cm}^{-3}$.)

Anisotropic thermal-conductivity characterisation with thermography

Having measured the heat capacity, it becomes possible to measure the effective thermal conductivity within the battery cell by inverse modelling using numerical simulations. Generally the thermal response of the cell follows the heat equation. The form

$$\frac{C_p^{\text{battery}}}{V^{\text{battery}}} \frac{\partial T}{\partial t} = \nabla \cdot (\mathbf{k} \cdot \nabla T) \tag{6}$$

applies when there is no internal heat generation within the battery. Note that this expression involves an effective thermal-conductivity tensor $\mathbf{k}$ to account for anisotropy. Obviously $\mathbf{k}$ is a homogenized quantity that combines the conductivities of current collectors, electrolyte, electrode materials, etc. This homogenization leads one to expect that $\mathbf{k}$ is anisotropic: aligning cartesian coordinates within the cell as depicted in Figure 2(c), the stacked electrode layers are normal to the x axis; consequently one expects the thermal conductivity in the y-z plane to differ from the thermal conductivity in the x direction. We assume that the thermal-conductivity tensor is diagonal when the axes are oriented as in Figure 2(c), so that the only non-zero components of $\mathbf{k}$ are k_{xx}, k_{yy}, and k_{zz}, and consequently

$$\frac{C_p^{\text{battery}}}{V^{\text{battery}}} \frac{\partial T}{\partial t} = k_{xx} \frac{\partial^2 T}{\partial x^2} + k_{yy} \frac{\partial^2 T}{\partial y^2} + k_{zz} \frac{\partial^2 T}{\partial z^2}. \tag{7}$$

This equation was solved to model an experiment in which a battery was heated from one side using a small disk-shaped heater, embedded in a thermal insulator.

The experimental geometry is shown schematically in Figure 2(a). Pouch cells for testing were laid horizontally on a cell holder. A custom-built circular polyimide heater (24 mm diameter × 0.4 mm thickness) was affixed to the geometric centre of the largest rectangular face of the cell, which was oriented downward. A thermocouple (Type K, Omega Engineering), which had previously been calibrated, was placed at the centre of the heater. This whole back surface was then well insulated with Armaflex insulation material (Class O, $0.02\ \text{W m}^{-1}\text{K}^{-1}$), held against the cell surface by tape. Finally, a thermal imaging camera (A655sc, FLIR Systems) was fixed at

Research Article
doi.org/10.1002/batt.202100401
Chemistry Europe
European Chemical Societies Publishing

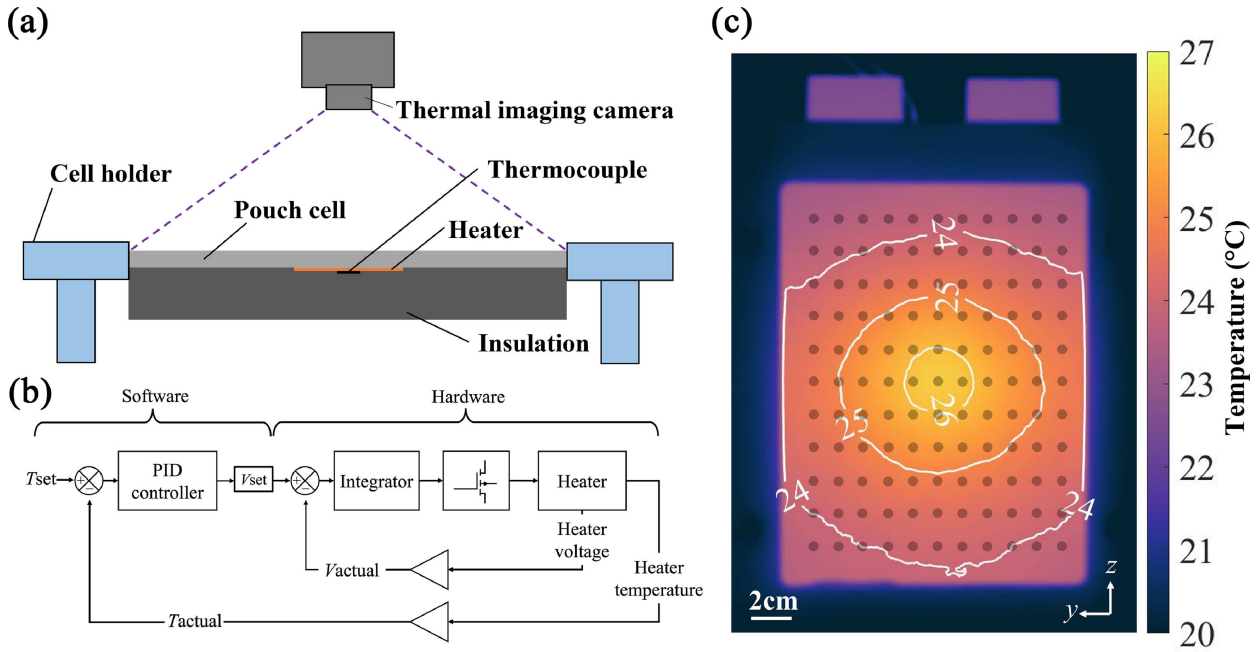

Figure 2. Thermal conductivity measurement using a spot-heated cell and infrared thermography. (a) Experimental schematic (side view). (b) Block diagram of control and data acquisition scheme. (c) Thermogram of the battery surface during an experiment, showing temperature contours in °C (x-axis into the page). The thermogram also indicates the position of the 11 × 11 grid along which temperature measurements were gathered. The central gridpoint is positioned directly across from the centre of the heater's surface.

the top of the test rig to record the transient surface-temperature response upon heating. Two RTD probes (1/10 DIN accuracy, Omega Engineering) were positioned near the cell holder to record the ambient temperature and were used as a reference for the camera. The heater was connected to a bespoke control circuit following the method of Howey et al.,[36] which regulated power to ensure a constant surface temperature. Taking the thermocouple reading as the feedback signal, a proportional–integral–derivative (PID) control program was executed in Labview to fix a constant thermocouple temperature as per the block diagram in Figure 2(b). The temperature setpoint was generally reached on a very short timescale (order seconds).

To model this configuration, energy-balance equation 7 was simulated with a constant-temperature boundary condition (Dirichlet type) where the heater contacted the back of the battery cell; an adiabatic (Neumann type) boundary condition on the rest of the back; and Newton's law of cooling (Robin type) on all of the remaining exterior surfaces of the cell. In mathematical terms,

$$\begin{aligned} T &= T_{\mathrm{h}} && (\text{Dirichlet}),\\ -\vec{n}\cdot\mathbf{k}\cdot\nabla T &= 0 && (\text{Neumann}),\\ -\vec{n}\cdot\mathbf{k}\cdot\nabla T &= h(T-T_{\mathrm{a}}) && (\text{Robin}), \end{aligned} \tag{8}$$

where T_{h} is the heater's surface temperature, h is a heat-transfer coefficient ostensibly describing free convection, and $\vec{n}$ is an outward surface normal vector; $\mathbf{k}$ represents the diagonal thermal-conductivity tensor.

The thermal model was solved numerically with COMSOL Multiphysics software, assuming that the battery was initially at ambient temperature, and using the actual T_{h} values recorded by the heater's controller as a transient Dirichlet condition. Source code is available on GitHub.[37] These simulations produce the transient temperature distribution on the surface of the cell opposite the heater as a function of the ambient temperature, heat-transfer coefficient, volumetric battery heat capacity, and the three diagonal thermal-conductivity tensor components.

To fit the thermal conductivity, a uniform 11 × 11 matrix of surface temperature points was defined around the heater centre, evenly spaced as shown in Figure 2(c), for a total of 121 points across the cell surface. To quantify the discrepancy between simulation and experiment, an objective function f was defined as

$$f = \sum_{i=1}^{11}\sum_{j=1}^{11}\sum_{k=1}^{N}\left(\frac{T_{ijk}^{\mathrm{sim}} - T_{ijk}^{\mathrm{exp}}}{T_{ijk}^{\mathrm{exp}}}\right)^2 \tag{9}$$

where indices i,j designate locations on the surface grid and k is the time step; N is the number of data sets in the time series. During fitting, the components of thermal conductivity and the heat-transfer coefficient were adjusted to minimize f via a nonlinear least-squares optimization algorithm.

Research Article
doi.org/10.1002/batt.202100401
Chemistry Europe
European Chemical Societies Publishing

Results and Discussion

Heat capacity

Heat-capacity measurements were always performed in pairs; for each run, a reference step with dielectric fluid alone was carried out prior to each test step with a sample. The empty chamber was typically rested for more than an hour between pairs of runs. For both reference and test steps, the dielectric fluid was initially heated to *ca.* 45 °C before being transferred to the insulated box, after which its tare weight was recorded. The pouch cell was always at ambient temperature (ca. 25–28 °C) before being immersed in the fluid; test data were only processed after the battery-surface and fluid temperatures equilibrated (cf. Figure 1). Figure 3 illustrates the temperature responses of the apparatus during the reference and test steps of Run #1 as an example. Reference and test data during the thermal equilibrium period established during the test step (cf. Figure 1(b)) are plotted on a semi-log scale. Linear fits are provided for comparison, confirming the expectations that the thermal relaxation is linear in the semi-log representation, and also that temperature in the test step decays with a shallower slope. Four runs of the experiment were performed, yielding the heat-capacity measurements in Table 1. The heat capacity of the cell was 541 JK^{-1}; standard error of the mean across the four runs was 13 JK^{-1}, approximately 2.4%.

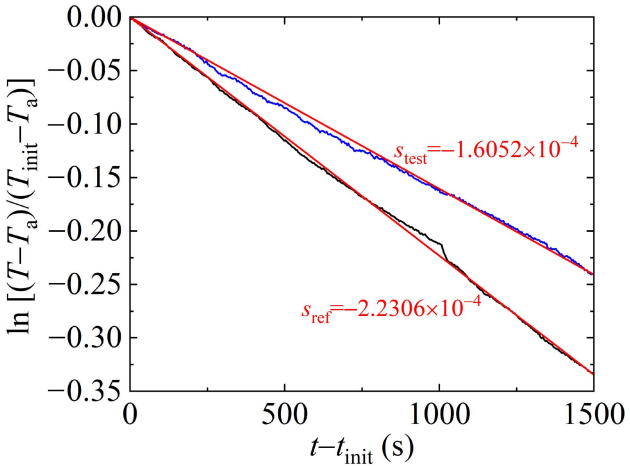

Figure 3. Run #1 of specific-heat measurement by transient cooling for a pouch cell, showing the temperature responses during reference (black) and test steps (blue). Linear fits for each test are shown in red.

To validate the method, an aluminium alloy (Grade 5251-H22) plate with similar dimensions to the pouch cell (205 × 161 × 6 mm) was also studied with the transient cooling apparatus. The density, specific heat and thermal conductivity of the aluminium alloy have been reported previously as 2690 $kg\,m^{-3}$, 900 $J\,kg^{-1}\,K^{-1}$ and 149 $W\,m^{-1}\,K^{-1}$, respectively.[38,39] Table 1 also presents data from four transient-cooling runs using the aluminium plate as a test sample instead of the battery.

The average specific heat of the Al plate was found to be 0.908 $J\,g^{-1}\,K^{-1}$, with standard error of the mean of 0.011 $J\,g^{-1}\,K^{-1}$, or 1.2%. Note that this standard error, despite being small, is greater than the 1% deviation of the measured heat capacity from the literature value for aluminium. Thus our best estimate of heat capacity for aluminium agrees with the literature value within the experimental error. Runs with the LFP pouch cell at 100% SOC yield an average heat capacity of 541 JK^{-1}, with a standard error of the mean of 13 JK^{-1} (2.4%).

Note that runs were also conducted with the cell at 50% SOC; these results are provided in Table S1 of the supplementary information. The cell's heat capacity at 50% SOC was 507 JK^{-1} with standard error of 1.8%, i.e. 9 JK^{-1}. These data are suggestive, but more experiments would be required to conclude decisively whether the pouch cell's heat capacity varies significantly with SOC.

Previous studies have reported specific heat capacities of LFP cells, which are compared to the present results in Table 2. These values range from 0.95 to 1.70 $J\,g^{-1}\,K^{-1}$; the majority are near 1 $J\,g^{-1}\,K^{-1}$. Given that the specific heat capacity at 100% SOC is 1.11 ± 0.05 $J\,g^{-}\,K^{-1}$, the present method yields results in good agreement with prior observations.

Thermal conductivity

Thermal-conductivity measurements were made by recording the transient thermography response of the cell surface to a step change in heater temperature. At the beginning of each run, the heater was stepped from ambient temperature up to 50 °C. Thermograms of the cell surface, as well as heater voltage, current and temperature, were recorded at 1 s

Table 1. Heat capacity of the aluminium reference sample and LFP pouch cell @100% SOC.

Sample	Run	Reference[a] m_f^{ref} [g]	s^{ref} [10^{-4} s^{-1}]	Test[b] m_f^{test} [g]	s^{test} [10^{-4} s^{-1}]	Heat capacity C_p [JK^{-1}]	$\hat{C}_p$ [$Jg^{-1}K^{-1}$]
Al plate	1	969.6	2.7225	1001.6	2.0063	474.2	0.8890
	2	1027.1	2.6461	917.1	2.2031	478.0	0.8961
	3	891.6	2.8467	937.6	1.9991	501.4	0.9400
	4	948.7	2.8003	936.4	2.1132	484.4	0.9081
Battery	1	990.4	2.2306	1000.8	1.6052	567.0	1.1596
	2	1021.1	2.3034	989.4	1.7756	506.2	1.0352
	3	992.3	2.1798	1003.2	1.5797	552.7	1.1305
	4	1013.4	2.2198	991.5	1.6702	536.6	1.0972

[a] The masses of the Al plate and battery are 533.4 g and 489.0 g, respectively. [b] The specific heat of the dielectric fluid is 1.510 $J\,g^{-1}\,K^{-1}$ at 20–40 °C, provided by the manufacturer.

Research Article
doi.org/10.1002/batt.202100401
Chemistry Europe
European Chemical Societies Publishing

Table 2. Specific heat capacities reported for LFP/graphite cells.

Authors	Cell geometry	Capacity [Ah]	Method	$\hat{C}_p$ [J g^{-1} K^{-1}]
Prada et al.[40]	Cylindrical	2.3	Accelerating rate calorimetry	1.100
Fleckenstein et al.[23]	Cylindrical	4.4	Thermal impedance spectroscopy	0.958
Bazinski et al.[18]	Pouch	14	Accelerating rate calorimetry	1.10–1.68
Bryden et al.[19]	Cylindrical	2.5	Internal temperature sensors	1.169
Sheng et al.[33]	Prismatic	8	Improved calorimetry	1.08–1.27
Chu et al.[16]	Pouch (various SOC)	20	Lock-in thermography	0.93–1.06
This work	Pouch (100% SOC)	20	Transient cooling	1.10

intervals. Each test had a total duration of 900 s. The aluminium reference sample was used to validate the thermal-conductivity measurement approach. Table 3 presents the estimated thermal conductivity k from each of these tests, gathered under the assumption that the thermal conductivity of aluminium is isotropic ($k_{xx} = k_{yy} = k_{zz}$ in **k**). The mean is 144 W m^{-1} K^{-1} and the standard deviation of the mean is 1.3 W m^{-1} K^{-1} (0.9%). Similarly the mean estimated heat-transfer coefficient is 15.4 W m^{-2} K^{-1}, with a standard deviation of the mean of 0.35 W m^{-2} K^{-1} (2.3%). These numbers reasonably agree with literature for aluminium alloy 5251 (k = 149 W m^{-1} K^{-1})[38] and heat transfer for free convection from a flat plate (h = 2–25 W m^{-2} K^{-1}).[41]

Table 3. Thermal conductivity of the aluminium plate.

Test number	k [W m^{-1} K^{-1}]	h [W m^{-2} K^{-1}]
1	141	15.2
2	143	14.7
3	147	15.4
4	145	16.4

Next, identical thermography experiments were conducted on the lithium-ion pouch cell at 100% SOC. Figure 4(a) shows the typical evolution of temperature on the exposed cell surface yielded by thermography, and Figure 4(b) shows the best-fit model results for comparison. Figure 4(c) presents plots of the transient temperatures at various points across the cell

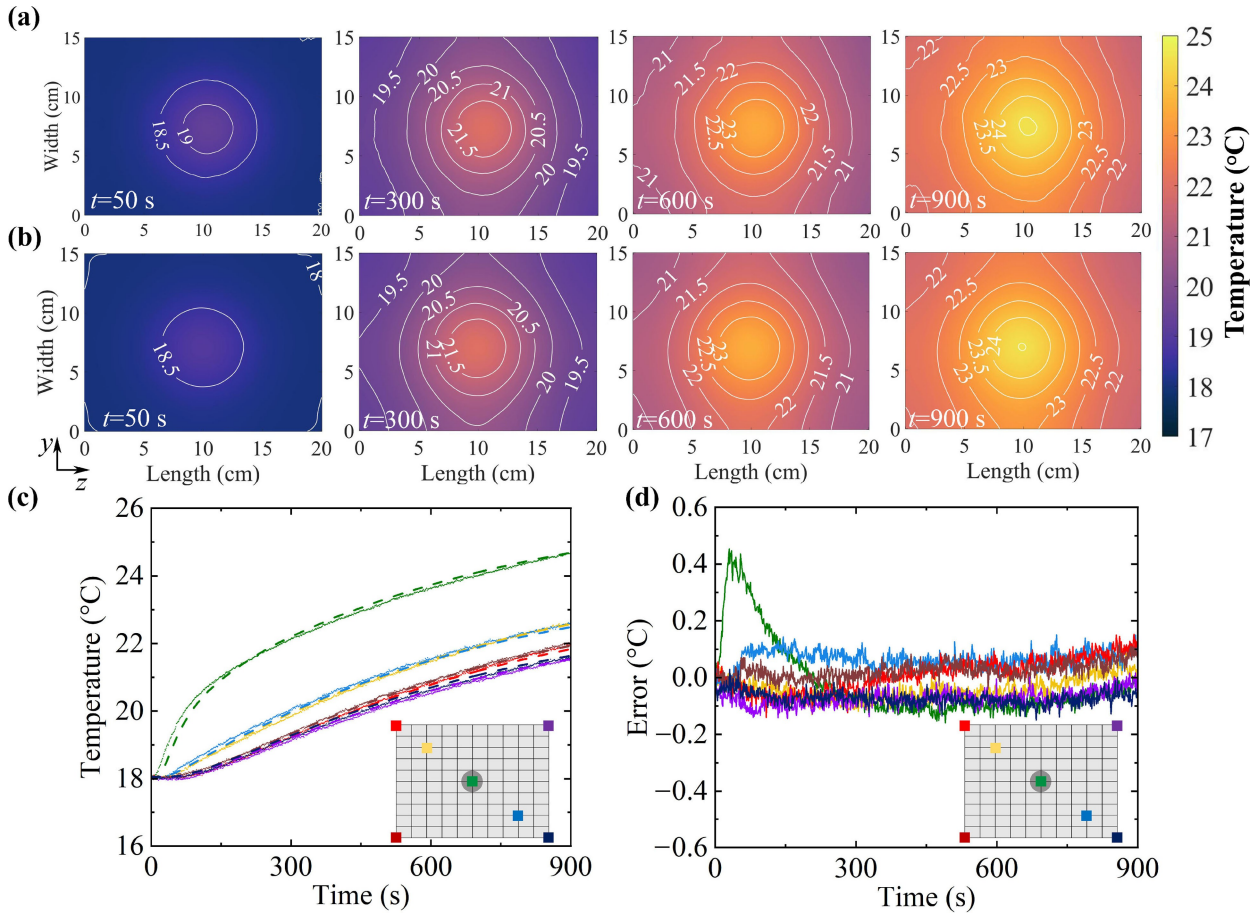

Figure 4. Test #1 of the thermal-conductivity characterisation. (a) Thermal images of cell front surface at t =50 s, 300 s, 600 s and 900 s. (b) Simulation output with best-fit parameters based on the experiment shown in panel (a); note that the tabs are at the right edge of the images. Measured (points) and simulated (dashed lines) surface-temperature data (c) and experimental error (d) at selected locations colour-coded in the insets.

surface. As expected, the position on the exposed surface directly opposite the centre of the heating element is always hottest. Its temperature does not begin to rise until about 50 s after the heater is switched on, because some time is taken for the thermal boundary layer to travel through the pouch. This lag time depends directly on the through-plane thermal conductivity component k_{xx}. Notably, the shapes of the temperature contours at short times (50 s) are reasonably circular, indicating that the thermal-conductivity components in-plane (in the y and z directions) are nearly equal. At longer times, the temperature rises across the entire cell surface. Rather than exhibiting boundary-layer behaviour, the point directly opposite the heater centre begins to relax exponentially upwards, towards a steady-state temperature. During this time, the temperature profile also spreads beyond the heater's position due to in-plane heat conduction. The temperature contours at longer times (after 300 s) deviate from circularity because of edge effects – i.e., due to a difference in the cooling rates between the short and long cell edges. Notably, the lag time after which temperature begins to rise at a given point on the surface increases with respect to the point's distance from the centre of the heater, because the thermal boundary layer must travel further to reach it. Finally, it is observed that the temperature on the side near the tabs (the right of the thermograms in Figure 4) differs slightly from that on the left. This owes to direct conduction of heat through the tabs, which slightly alters the thermal boundary conditions.

Table 4 summarises the results of four thermal-conductivity measurements. The mean through-plane thermal conductivity k_{xx} was 0.51 $W m^{-1} K^{-1}$, with a standard error of 1.8%. This is about 50 times smaller than the in-plane thermal conductivities, $k_{yy} = 26.45\ W m^{-1} K^{-1} \pm 1.5\%$ and $k_{zz} = 26.75\ W m^{-1} K^{-1} \pm 1.7\%$. Notably the in-plane conductivity components agree within the experimental error, but the through-plane conductivity component differs significantly. Therefore the in-plane conductivity $k_{\parallel}$ will be treated as a single quantity, $k_{yy} = k_{zz} = k_{\parallel}$ henceforth. Under this assumption the experimental in-plane conductivity was found to be $k_{\parallel} = 26.6\ W m^{-1} K^{-1} \pm 1.1\%$.

To probe the SOC dependence of thermal conductivity, additional measurements were carried out at 50% SOC. Results of these experiments are presented in Table S2 of the Supplementary Information. The average k_{xx}, k_{yy} and k_{zz} did not change beyond the bounds of experimental error.

The through-plane and in-plane thermal conductivity measured in this work are compared with previous studies in Table 5, showing fair agreement.

Table 4. Thermal conductivity components of the LFP pouch cell at 100% SOC.

Test number	k_{xx} [$W m^{-1} K^{-1}$]	k_{yy} [$W m^{-1} K^{-1}$]	k_{zz} [$W m^{-1} K^{-1}$]	h [$W m^{-2} K^{-1}$]
1	0.513	26.6	27.0	18.5
2	0.503	25.9	26.2	18.3
3	0.503	25.8	25.9	17.7
4	0.544	27.5	27.9	17.2

Conclusions

Novel methods were proposed and implemented to quantify heat capacity and three-dimensional thermal-conductivity components for large-format lithium-ion pouch cells. Heat capacity was measured by tracking the thermal relaxation of a diabatic calorimetry cell that enclosed a battery immersed in a hot working fluid. Newton's law of cooling was exploited to determine the heat capacity from the different relaxation times during reference and test steps. Subsequently, the anisotropic thermal-conductivity components were estimated by fitting a 3D finite-element model to the transient surface-temperature profiles imposed by a disc-shaped, isothermal heater in contact with the rear of the pouch cell. The front-surface temperature was monitored transiently by infrared thermography as the heater underwent a step change in temperature. In both cases, the accuracy of the technique was confirmed by comparing measurements of battery cells to measurements of an aluminium plate, for which all relevant properties were known.

Accurate values for a battery's heat capacity and thermal conductivity are crucial to thermal modelling, and are not widely reported. The characterisation methods presented here are simple to execute and could be useful to researchers who require values of thermal parameters. Experiments quantifying heat capacity and thermal-conductivity components were found to have good precision (within 1–3% across all experiments), as well as comparing well with the available literature data for LFP cells. Notably, anisotropic thermal-conductivity estimates are not broadly available in the battery literature. We find that considering this anisotropy is critical because the in-plane and through-plane conductivities differ by well over an order of magnitude; this has significant impact on thermal transients that should be considered within battery models. The state-of-charge dependence of thermal properties could also be worth considering in the future, but preliminary data

Table 5. Thermal conductivity of LFP/graphite cells reported in the literature.[a]

Authors	Cell geometry	Capacity [Ah]	Method	$k_{\perp}$ [W/(m·K)]	$k_{\parallel}$ [W/(m·K)]
Bazinski et al.[18]	Pouch	14	Constant heat flux	0.34–0.37	–
Vertiz et al.[20]	Pouch	14	Hot plate	0.235–0.284	–
Fleckenstein et al.[23]	Cylindrical	4.4	Thermal impedance spectroscopy	0.35	–
Drake et al.[32]	Cylindrical	–	Constant heat flux	0.15–0.20	30.4–32.0
This work	Pouch	20	Spot temperature-step transient	0.51	26.6

[a] Subscripts "⊥" and "||" denote the through-plane and in-plane directions, respectively.

here suggest that its importance is secondary. It would also be worthwhile to probe the temperature dependence of these properties.

Acknowledgment

The authors gratefully acknowledge funding from the EPSRC Translational Energy Storage Diagnostics (TRENDs) project (EP/R020973/1) and the STFC Futures Early Career Award, as well as the Faraday Institution Multiscale Modelling Project (subaward FIRG003 under grant EP/P003532/1). We are grateful to Peter Get from the Oxford Robotics Institute for constructing and testing the circuit used to drive the heater.

Conflict of Interest

The authors declare no conflict of interest.

Data Availability Statement

Data is available (as well as code) from GitHub, at https://github.com/Battery-Intelligence-Lab/battery-thermal-characterisation.

Keywords: lithium-ion battery · specific heat · thermal conductivity · cooling · thermography

[1] T. M. Gür, *Energy Environ. Sci.* **2018**, *11(10)*, 2696–2767.
[2] B. C. Gibb, *Nat. Chem.* **2021**, *13(2)*, 107–109.
[3] M. S. Ziegler, J. E. Trancik, *Energy Environ. Sci.* **2021**, *14(4)*, 1635–1651.
[4] S. Chu, Y. Cui, N. Liu, *Nat. Mater.* **2016**, *16(1)*, 16–22.
[5] Y. Zhu, J. Xie, A. Pei, B. Liu, Y. Wu, D. Lin, J. Li, H. Wang, H. Chen, J. Xu, A. Yang, C. L. Wu, H. Wang, W. Chen, Y. Cui, *Nat. Commun.* **2019**, *10(1)*, 2067.
[6] D. P. Finegan, M. Scheel, J. B. Robinson, B. Tjaden, I. Hunt, T. J. Mason, J. Millichamp, M. Di Michiel, G. J. Offer, G. Hinds, D. J. L. Brett, P. R. Shearing, *Nat. Commun.* **2015**, *6*, 6924.
[7] X. Feng, M. Ouyang, X. Liu, L. Lu, Y. Xia, X. He, *Energy Storage Mater.* **2018**, *10*, 246–267.
[8] J. Lin, H. N Chu, D. A. Howey, C. W Monroe, Multiscale coupling of surface temperature with solid diffusion in large lithium-ion pouch cells. *arXiv preprint:* https://arxiv.org/abs/2109.12903, **2021**.
[9] B. Koo, P. Goli, A. V. Sumant, P. C. dos Santos Claro, T. Rajh, C. S. Johnson, A. A. Balandin, E. V. Shevchenko, *ACS Nano* **2014**, *8(7)*, 7202–7207.
[10] T. Amietszajew, J. Fleming, A. J. Roberts, D. Widanalage, D. Greenwood, M. D. R. Kok, M. Pham, D. J. L. Brett, P. R. Shearing, R. Bhagat, *Batteries & Supercaps* **2019**, *2(11)*, 934–940.
[11] J. Huang, L. Albero Blanquer, J. Bonefacino, E. R. Logan, D. Alves Dalla Corte, C. Delacourt, B. M. Gallant, S. T. Boles, J. R. Dahn, H.-Y. Tam, J.-M. Tarascon, *Nat. Energy* **2020**, *5(9)*, 674–683.
[12] J. Xu, J. Chao, T. Li, T. Yan, S. Wu, M. Wu, B. Zhao, R. Wang, *ACS Cent. Sci.* **2020**.
[13] M. Heinrich, N. Wolff, N. Harting, V. Laue, F. Röder, S. Seitz, U. Krewer, *Batteries & Supercaps* **2019**, *2(6)*, 530–540.
[14] F. Röder, V. Laue, U. Krewer, *Batteries & Supercaps* **2019**, *2(3)*, 248–265.
[15] J. Deng, C. Bae, J. Marcicki, A. Masias, T. Miller, *Nat. Energy* **2018**, *3(4)*, 261–266.
[16] H. N. Chu, S. U. Kim, S. K. Rahimian, J. B. Siegel, C. W. Monroe, *J. Power Sources* **2020**, *453*, 227787.
[17] S. U. Kim, P. Albertus, D. Cook, C. W. Monroe, J. Christensen, *J. Power Sources* **2014**, *268*, 625–633.
[18] S. J. Bazinski, X. Wang, *J. Power Sources* **2015**, *293*, 283–291.
[19] T. S. Bryden, B. Dimitrov, G. Hilton, C. Ponce de León, P. Bugryniec, S. Brown, D. Cumming, A. Cruden, *J. Power Sources* **2018**, *395*, 369–378.
[20] G. Vertiz, M. Oyarbide, H. Macicior, O. Miguel, I. Cantero, P. Fernandez de Arroiabe, I. Ulacia, *J. Power Sources* **2014**, *272*, 476–484.
[21] D. Werner, A. Loges, D. J. Becker, T. Wetzel, *J. Power Sources* **2017**, *364*, 72–83.
[22] A. Loges, S. Herberger, P. Seegert, T. Wetzel, *J. Power Sources* **2016**, *336*, 341–350.
[23] M. Fleckenstein, S. Fischer, O. Bohlen, B. Bäker, *J. Power Sources* **2013**, *223*, 259–267.
[24] J. Zhang, B. Wu, Z. Li, J. Huang, *J. Power Sources* **2014**, *259*, 106–116.
[25] K. A. Murashko, A. V. Mityakov, J. Pyrhönen, V. Y. Mityakov, S. S. Sapozhnikov, *J. Power Sources* **2014**, *271*, 48–54.
[26] H. Maleki, *J. Electrochem. Soc.* **1999**, *146(3)*.
[27] H. Maleki, H. Wang, W. Porter, J. Hallmark, *J. Power Sources* **2014**, *263*, 223–230.
[28] A. Loges, S. Herberger, D. Werner, T. Wetzel, *J. Power Sources* **2016**, *325*, 104–115.
[29] A. J. Schmidt, X. Chen, G. Chen, *Rev. Sci. Instrum.* **2008**, *79(11)*, 114902.
[30] K. Jagannadham, *J. Power Sources* **2016**, *327*, 565–572.
[31] F. Richter, S. Kjelstrup, P. J. S. Vie, O. S. Burheim, *J. Power Sources* **2017**, *359*, 592–600.
[32] S. J. Drake, D. A. Wetz, J. K. Ostanek, S. P. Miller, J. M. Heinzel, A. Jain, *J. Power Sources* **2014**, *252*, 298–304.
[33] L. Sheng, L. Su, H. Zhang, Y. Fang, H. Xu, W. Ye, *Energy Convers. Manage.* **2019**, *180*, 724–732.
[34] X. Zhang, R. Klein, A. Subbaraman, Sergei Chumakov, X. Li, J. Christensen, C. Linder, S. U. Kim, *J. Power Sources* **2019**, *412*, 552–558.
[35] Julabo. *Thermal H10 data sheet*, 2020.
[36] D. A. Howey, A. S. Holmes, K. R. Pullen, *Int. J. Heat Mass Transfer* **2010**, *53(1-3)*, 491–501.
[37] J. Lin, H. N. Chu, C. W. Monroe, D. A. Howey. Anisotropic thermal-conductivity characterisation with thermography. https://github.com/Battery-Intelligence-Lab/battery-thermal-characterisation, **2021**.
[38] Smiths Metal Centres. *5251 (NS4) Aluminium Alloy Technical Datasheet*, **2018**.
[39] MakeItFrom Material Properties Database. *5251-H22 Aluminium*, **2020**.
[40] E. Prada, D. Di Domenico, Y. Creff, J. Bernard, V. Sauvant-Moynot, F. Huet, *J. Electrochem. Soc.* **2012**, *159(9)*, A1508–A1519.
[41] T. L. Bergman, F. P. Incropera, A. S. Lavine, *Fundamentals of heat and mass transfer.* John Wiley & Sons, **2011**.

Manuscript received: December 20, 2021
Revised manuscript received: January 31, 2022
Accepted manuscript online: February 3, 2022
Version of record online: March 4, 2022